Non-reflecting Boundary Conditions for Updated Lagrangian Hydrodynamics Simulations

N. Therme[1,2], S. Guisset[1,2]

Abstract

This paper presents a non-reflecting boundary condition (NRBC) strategy specifically designed for compressible flow simulations within an updated Lagrangian hydrodynamic framework. The method is grounded in the characteristic decomposition of the linearized Euler equations, extending the approach pioneered by Giles [5]. By analyzing the local eigenstructure of the system, incoming and outgoing waves are precisely identified at the domain boundaries. This identification enables the selective suppression of incoming waves, effectively preventing unwanted reflections. A key advantage of this NRBC approach is its full compatibility with all standard updated Lagrangian schemes, whether staggered or cell-centered. The practical implementation of the NRBC is discussed in detail. Numerical experiments conducted on one-dimensional and two-dimensional problems demonstrate the method's effectiveness in absorbing outgoing disturbances, confirming its non-reflecting properties.

Key words: Non-reflecting boundary conditions, Lagrangian hydrodynamics, characteristics method, numerical simulations.

1 Introduction

The comprehensive simulation of complex physical phenomena or industrial applications of practical interest often exceeds the computational capabilities of current numerical methods and available resources. To circumvent

[1]CEA/CESTA, 15 Avenue des Sablières CS 60001, 33116 Le Barp cedex, France
[2]nicolas.therme@cea.fr / sebastien.guisset@cea.fr

these limitations, computational strategies typically involve focusing on localized regions where the phenomena of interest occur, allowing for refined mesh resolution to accurately capture the underlying physical processes. This domain decomposition approach, while computationally efficient, inevitably requires the introduction of artificial boundaries that truncate the original problem domain. Such boundary truncation can significantly compromise solution accuracy, as spurious wave reflections at these artificial interfaces may propagate back into the computational domain and contaminate the physical solution. To preserve numerical fidelity, it is therefore crucial to implement appropriate boundary treatments that ensure outgoing waves are effectively absorbed without generating non-physical reflections, thereby maintaining the integrity of the solution within the region of computational interest. In this context, the past decades have witnessed the development of non-reflecting boundary conditions for simulating wave propagation in refined computational subdomains.

A seminal contribution was made by Engquist and Majda [3], who pioneered the development of exact and approximate boundary conditions for hyperbolic partial differential equations. Their work was subsequently expanded to include the simulation of acoustic and elastic waves [4]. Furthermore, Giles [5] introduced non-reflecting boundary conditions (NRBCs) for the Euler equations, thereby extending the applicability of the NRBC methodology to compressible flow simulations. Additionally, the study of compressible viscous flows was addressed in [15]. A comprehensive early review of NRBC development, covering both theoretical and numerical aspects, can be found in [6]. More recent research has concentrated on the development of high-order boundary treatments [7] and the adaptation of standard NRBC concepts to alternative numerical frameworks [11]. While NRBCs have been thoroughly explored within the Eulerian framework, their application and practical implementation in updated Lagrangian approaches remain relatively underexplored.

Two fundamental kinematic frameworks are used to describe fluid and solid motion: the Eulerian and the Lagrangian descriptions. In the Eulerian framework, the conservation laws are formulated with respect to a fixed spatial reference frame. In contrast, the Lagrangian approach formulates these laws in a reference frame that moves with the material, thereby following the trajectories of individual fluid or solid particles. The Lagrangian formulation is particularly popular as it offers a natural and precise framework for tracking material interfaces. This feature is especially advantageous for

the simulation of multi-material compressible flows. In this framework, one must discretize the conservation equations as well as the vertex motion in order to move the mesh (cells used for the numerical simulation). Over the past decades, several numerical methods have been designed to solve the Lagrangian hydrodynamic equations. In this introduction, we restrict ourselves to mentioning two of the most popular ones. A first popular class of numerical methods consists of "staggered schemes" [16, 17] in which the kinematic variables (node velocities and node positions) are computed at the nodes while the thermodynamic quantities (density and internal energy) are evaluated at the centers of the cells. A second category consists of "cell-centered finite volume schemes". These schemes are based on the pioneering work of Godunov [8] and consider cell-centered quantities. In this case, the node velocities are obtained from a nodal solver. Over the years, various multi-directional extensions have been proposed [2, 12, 1, 9]. We note that the NRBC strategy proposed in this work is compatible with both categories, rendering the approach particularly versatile and of broad interest to the community.

The NRBC method presented in this document is largely inspired by the approach developed by Giles [5] for the Euler equations (Eulerian formalism), where perturbative and characteristic wave analyses are used to cancel the incoming wave components at artificial boundaries. Giles's formulation has become very popular for Eulerian computational fluid dynamics simulations; however, its adaptation to the updated Lagrangian framework with its practical implementation is far less common. To our knowledge, this topic, with clear numerical comparisons with regard to standard Neumann boundary conditions, has not been addressed in the literature. The standard Neumann boundary conditions, often used for their simplicity, do not distinguish between incoming and outgoing wave components. As a result, these boundary conditions may lead to unwanted wave reflections that degrade the numerical solution near the domain boundaries. Applying a characteristic-based NRBC in the updated Lagrangian context is therefore both technically interesting and practically valuable for physical application simulations.

The present document is organized as follows. Section 2 presents the mathematical formulation of the updated Lagrangian governing equations with the hypo-elasticity and the pure hydrodynamics models. In Section 3, the derivation of the non-reflecting boundary condition (NRBC) inspired by Giles' approach [5] is detailed for the updated Lagrangian model. Section 4 discusses how the components linked to the incoming characteristics are

canceled and the associated numerical implementation to enforce this condition. Section 5 provides several validation results that compare the proposed NRBC method against the standard Neumann boundary conditions. This last section demonstrates its effectiveness in suppressing spurious reflections. Finally, our conclusion is given with a summary of key findings and suggestions for future research directions.

2 Governing equations

The system of conservation laws describing an elastic material is the system of Euler equations with the Cauchy stress tensor $\mathbb{T}$. This tensor is symmetric, i.e., $\mathbb{T} = \mathbb{T}^t$, and we denote by ρ the solid density, $\boldsymbol{V}$ its velocity, and E its specific total energy. The updated Lagrangian form of this system writes as follows:

$$\begin{cases} \rho \dfrac{d}{dt}\left(\dfrac{1}{\rho}\right) = \nabla \cdot \boldsymbol{V}, \\ \quad \rho \dfrac{d}{dt}\boldsymbol{V} = -\nabla \cdot \mathbb{T}, \\ \quad \rho \dfrac{d}{dt}E = -\nabla \cdot (\mathbb{T}\boldsymbol{V}), \end{cases} \tag{1}$$

with the notation $\dfrac{d}{dt}\cdot = \dfrac{\partial}{\partial t}\cdot + \boldsymbol{V} \cdot \nabla \cdot$. These equations correspond respectively to the conservation of mass, momentum, and specific total energy, and the specific internal energy writes $\varepsilon = E - \frac{1}{2}\boldsymbol{V}^2$. In order to close the system, the thermodynamic variables and the Cauchy stress tensor must be related. This aspect will be detailed in the next section.

Hypo-elasticity model

The Cauchy stress tensor is symmetric, i.e., $\mathbb{T} = \mathbb{T}^t$, where the superscript t denotes the transpose operator. The stress tensor is decomposed into a hydrostatic component p and a deviatoric component S by setting

$$\mathbb{T} = -p\mathbb{I} + \mathbb{S}, \tag{2}$$

where p denotes the hydrodynamic pressure, $\mathbb{I}$ is the identity tensor, and $\mathbb{S}$ is the deviatoric part of the stress tensor. The equation of state for the

hydrodynamic component is introduced by expressing the material pressure in terms of the density and the specific internal energy:

$$p = p(\rho, \varepsilon). \tag{3}$$

The material evolution equation for the deviatoric stress $\mathbb{S}$ is given by an incremental constitutive law that applies to elastic-perfectly plastic materials. First, let us introduce some notation that will be useful for the expression of the constitutive equation. We denote by $\mathbb{D}$ the strain rate tensor, i.e., the symmetric part of the velocity gradient, defined by

$$\mathbb{D} = \frac{1}{2}\left(\nabla \boldsymbol{V} + (\nabla \boldsymbol{V})^t\right). \tag{4}$$

The incremental constitutive law for the material deviatoric stress writes as follows [17]:

$$\frac{d\mathbb{S}}{dt} = 2\mu\left(\mathbb{D}_0 - \mathbb{D}_p\right) - \left(\mathbb{S}\mathbb{W} - \mathbb{W}\mathbb{S}\right), \tag{5}$$

where μ is the Lamé coefficient, D_0 denotes the deviatoric part of the strain rate tensor D, which reads

$$\mathbb{D}_0 = \mathbb{D} - \frac{1}{3}\mathrm{tr}(\mathbb{D})\mathbb{I}, \tag{6}$$

where tr denotes the standard trace operator (sum of the elements on the diagonal). Finally, $\mathbb{W}$ corresponds to the antisymmetric part of the velocity gradient (spin tensor):

$$\mathbb{W} = \frac{1}{2}\left(\nabla \boldsymbol{V} - (\nabla \boldsymbol{V})^t\right). \tag{7}$$

The deviatoric stress $\mathbb{S}$ is subjected to the plastic boundedness inequality:

$$f = \sqrt{\mathbb{S} : \mathbb{S}} - \sqrt{\frac{2}{3}} Y_0 \leq 0, \tag{8}$$

where f is the yield function and Y_0 is the material yield strength, which is a constant in the case of elastic-perfectly plastic materials. The last term in the incremental stress-strain equation (5) ensures that the constitutive law obeys the principle of material frame independence [10]. In the present study, the materials under consideration in the test section are characterized

by a Mie-Grüneisen equation of state. For a given specific internal energy and specific volume $V = 1/\rho$, the Mie-Grüneisen equation of state defines the pressure as follows:

$$p(V,\varepsilon) = \frac{a_0^2(V_0 - V)}{\left[V_0 - s\,(V_0 - V)\right]^2} + \frac{\Gamma(V)}{V}\left[\varepsilon - \frac{1}{2}\left(\frac{a_0\,(V_0 - V)}{V_0 - s\,(V_0 - V)}\right)^2\right], \quad (9)$$

where $V_0 = 1/\rho_0$ corresponds to the specific volume of the unstressed material. Referring to [13], the physical coefficients a_0 and s need to be defined and link the shock speed in the material U_s with the velocity u_p (material velocity behind the shock front) by an empirically obtained linear relationship $U_s = a_0 + s\,u_p$. The Grüneisen parameter Γ is defined as follows:

$$\Gamma = V\left(\frac{\partial p}{\partial \varepsilon}\right)_V = \Gamma_0 \frac{V}{V_0}. \quad (10)$$

Following [14], this equation of state is rewritten in the following form for easier numerical implementation:

$$p(\rho,\varepsilon) = \rho_0 a_0^2 f(\eta) + \rho_0 \Gamma_0 \varepsilon, \quad (11)$$

where

$$\eta = \frac{\rho}{\rho_0}, \quad f(\eta) = \frac{(\eta - 1)[\eta - \Gamma_0(\eta - 1)/2]}{(\eta - s(\eta - 1))^2}. \quad (12)$$

Finally, for a general equation of state considered in the form $p = p(\rho,\varepsilon)$, the isentropic sound speed a is defined by

$$a^2 = \left(\frac{\partial p}{\partial \rho}\right)_\varepsilon + \frac{p}{\rho^2}\left(\frac{\partial p}{\partial \varepsilon}\right)_\rho. \quad (13)$$

When applying this last equation to the Mie-Grüneisen equation of state, one obtains

$$a^2 = a_0^2 f'(\eta) + \frac{\Gamma_0}{\rho_0}\frac{p}{\eta^2}, \quad f'(\eta) = \frac{\eta + (s - \Gamma_0)(\eta - 1)}{(\eta - s(\eta - 1))^3}. \quad (14)$$

Pure hydrodynamics model

In the case of pure hydrodynamics modeling, the stress tensor simplifies to

the hydrostatic component p (hydrodynamic pressure) while the deviatoric component S is set to zero:

$$\mathbb{T} = -p\mathbb{I}, \quad \mathbb{S} = 0. \tag{15}$$

In this document, the pure hydrodynamics tests presented in the numerical test section are restricted to perfect gas equations of state, which write as follows:

$$p = (\gamma - 1)\rho\varepsilon, \tag{16}$$

where the coefficient γ is known as the polytropic index of the gas. The corresponding expression of the speed of sound reads

$$a^2 = \gamma \frac{p}{\rho}. \tag{17}$$

3 Characteristic-based non-reflecting boundary conditions

In this section, the NRBC methodology is detailed. The derivation of the system linearization is presented, followed by the associated characteristic wave problem. By enforcing the cancellation of incoming characteristics, a NRBC condition is derived. The practical implementation is also discussed.

3.1 System linearization

The strategy is first detailed in a 1D setting in the pure hydrodynamics case but will later be applied in the general case. In this simplified framework, the set of equations rewrites

$$\begin{cases} \dfrac{d}{dt}\tau = \partial_m V, \\ \dfrac{d}{dt}V = -\partial_m p, \\ \dfrac{d}{dt}E = -\partial_m \left(pV\right), \end{cases} \tag{18}$$

where we have introduced the standard notations $\tau = 1/\rho$ and $\partial_m \cdot = \rho \partial_x \cdot$. We start by rewriting the system in terms of the variable $\mathbf{W} = (\tau, V, p)$. In

the case of regular solutions (non-dissipative solutions), the set of equations rewrites in non-conservative form:

$$\frac{d}{dt}\mathbf{W} + \mathbb{A}(\mathbf{W})\partial_m \mathbf{W} = \mathbf{0}, \tag{19}$$

with the Jacobian matrix

$$\mathbb{A}(\mathbf{W}) = \begin{pmatrix} 0 & -1 & 0 \\ 0 & 0 & 1 \\ 0 & a^2/\tau^2 & 0 \end{pmatrix}, \tag{20}$$

and the isentropic sound speed a is defined by

$$a^2 = \left(\frac{\partial p}{\partial \rho}\right)_{\varepsilon} = -\tau^2 \left(\frac{\partial p}{\partial \tau}\right)_{\varepsilon}. \tag{21}$$

We define the acoustic impedance

$$Z = a/\tau, \tag{22}$$

so the associated wave structure is given by the following three eigenvalues:

$$\lambda^- = -Z, \quad \lambda^0 = 0, \quad \lambda^+ = Z, \tag{23}$$

associated with the left eigenvectors

$$\mathbf{W}_L^- = (0 \quad -Z \quad 1), \quad \mathbf{W}_L^0 = \begin{pmatrix} Z^2 & 0 & 1 \end{pmatrix}, \quad \mathbf{W}_L^+ = (0 \quad Z \quad 1). \tag{24}$$

To derive the NRBC conditions, we employ a perturbative approach around a reference solution. The key idea is to linearize the system around a known reference state and analyze the propagation of small perturbations. Following this perturbative approach, the solution is expanded as follows:

$$\mathbf{W} = \mathbf{W}^{\text{ref}} + \varepsilon \tilde{\mathbf{W}}, \tag{25}$$

where $\mathbf{W}^{\text{ref}} = (\tau^{\text{ref}}, V^{\text{ref}}, p^{\text{ref}})$ represents a reference state that satisfies the original system of equations. The perturbation vector $\tilde{\mathbf{W}} = (\tilde{\tau}, \tilde{V}, \tilde{p})$ represents small deviations from this reference state, and ε is a small dimensionless parameter that characterizes the amplitude of the perturbations.

Substituting this expansion into the non-conservative form of the equations and neglecting terms of order ε^2 and higher, we obtain the linearized system governing the evolution of perturbations:

$$\frac{d}{dt}\tilde{\mathbf{W}} + \mathbb{A}(\mathbf{W}^{\text{ref}})\partial_m \tilde{\mathbf{W}} = \mathbf{0}. \tag{26}$$

This linearization is valid under the assumption that the perturbations remain small compared to the reference state throughout the domain of interest. The Jacobian matrix $\mathbb{A}(\mathbf{W}^{\text{ref}})$ is now evaluated at the constant reference state, which simplifies the subsequent characteristic analysis. The perturbation vector can finally be expressed in the eigenvector basis:

$$\begin{pmatrix} \tilde{c}^0 \\ \tilde{c}^+ \\ \tilde{c}^- \end{pmatrix} = \mathbb{B} \begin{pmatrix} \tilde{\tau} \\ \tilde{V} \\ \tilde{p} \end{pmatrix}, \quad \mathbb{B} = \begin{pmatrix} \mathbf{W}^0_{\text{ref},L} \\ \mathbf{W}^+_{\text{ref},L} \\ \mathbf{W}^-_{\text{ref},L} \end{pmatrix}. \tag{27}$$

3.2 Characteristic waves and NRBC implementation

The methodology to derive the non-reflecting boundary condition consists of canceling the components linked to the incoming characteristics (waves associated with the negative eigenvalues) [5]. This approach is adapted to compute an external state in a ghost cell of a Lagrangian hydrodynamics simulation code.

We consider a low-order explicit scheme where the solution in the boundary cells is denoted with subscript b. To enable the computation of numerical fluxes at the domain boundary, we introduce a fictitious cell (ghost cell) adjacent to each boundary cell. The procedure to enforce the NRBC is as follows:

Step 1: Definition of the reference state.

The reference state at time t^n is chosen to be equal to the state in the ghost cell at the previous time step:

$$\mathbf{W}^{\text{ref},n} = \mathbf{W}^{\text{fict},n-1} = (\tau^{\text{ref},n}, V^{\text{ref},n}, p^{\text{ref},n}). \tag{28}$$

Remark. For the first time iteration (index $n = 1$), we initialize the algorithm by setting $\mathbf{W}^{\text{ref},1} = \mathbf{W}^1_b$.

Step 2: Computation of the perturbation at the domain boundary.

The perturbation in the last cell of the domain (cell associated with the ghost cell) is defined as the difference between the state at time t^n and the reference state:

$$\begin{pmatrix} \Delta\tau_b \\ \Delta V_b \\ \Delta p_b \end{pmatrix}^n = \begin{pmatrix} \tau_b - \tau^{\text{ref}} \\ V_b - V^{\text{ref}} \\ p_b - p^{\text{ref}} \end{pmatrix}^n , \tag{29}$$

where $\mathbf{W}_b = (\tau_b, V_b, p_b)$ corresponds to the known solution at time t^n in the boundary cell of the computational domain.

Step 3: Projection onto the spectral basis.

This perturbation is projected onto the characteristic basis through the matrix B_b^n evaluated at the boundary cell state:

$$\begin{pmatrix} \tilde{c}_b^0 \\ \tilde{c}_b^+ \\ \tilde{c}_b^- \end{pmatrix} = \mathbb{B}_b^n \begin{pmatrix} \Delta\tau_b \\ \Delta V_b \\ \Delta p_b \end{pmatrix}^n . \tag{30}$$

The coefficients $\tilde{c}_b^-$, $\tilde{c}_b^0$, and $\tilde{c}_b^+$ are respectively the incoming, neutral, and outgoing characteristic components computed from the boundary cell perturbation.

Step 4: Propagation to the ghost cell and cancellation of the incoming characteristic.

It is assumed that the perturbation propagates into the ghost cell. Therefore, to satisfy the non-reflecting boundary condition, the component corresponding to the incoming characteristic is canceled by setting

$$\tilde{c}_b^- = 0. \tag{31}$$

Step 5: Ghost cell state determination.

The state in the ghost cell is computed by transforming the perturbation back to the original coordinate system. The values to be set in the ghost cell at time t^n are determined by

$$\begin{pmatrix} \tau^{\text{fict}} - \tau^{\text{ref}} \\ V^{\text{fict}} - V^{\text{ref}} \\ p^{\text{fict}} - p^{\text{ref}} \end{pmatrix}^n = \left(\mathbb{B}^{\text{fict},n}\right)^{-1} \begin{pmatrix} \tilde{c}_b^0 \\ \tilde{c}_b^+ \\ 0 \end{pmatrix}, \tag{32}$$

where $\mathbb{B}^{\text{fict},n}$ is the characteristic matrix evaluated at the fictitious state. Note that this choice results in solving a nonlinear problem.

Step 6: Detailed equation-by-equation formulation.

The system of equations (32) can be rewritten in explicit form as

$$\begin{cases} \tau^{\text{fict},n} - \tau^{\text{ref},n} = \dfrac{1}{\left(Z^{\text{fict},n}\right)^2}\left(\tilde{c}_b^0 - \dfrac{1}{2}\tilde{c}_b^+\right), \\ V^{\text{fict},n} - V^{\text{ref},n} = \dfrac{\tau^{\text{fict},n}\tilde{c}_b^+}{2a^{\text{fict},n}}, \\ p^{\text{fict},n} - p^{\text{ref},n} = \dfrac{\tilde{c}_b^+}{2}. \end{cases} \tag{33}$$

Due to the nonlinearity of the problem, an iterative algorithm is used in practice to solve the first equation of this system (nonlinear scalar equation). Once the value of $\tau^{\text{fict},n}$ is obtained, the computation of $V^{\text{fict},n}$ and $p^{\text{fict},n}$ is straightforward using the last two equations. Once the value of the fictitious pressure $p^{\text{fict},n}$ is known, the non-reflecting boundary condition is easily implemented. In the context of a cell-centered Lagrangian scheme, where a nodal solver balances the pressure forces acting around each mesh node, the effect of the boundary is accounted for by including the contribution of $p^{\text{fict},n}$. The fictitious pressure is treated as an additional pressure term applied at the boundary and incorporated into the force balance at the node adjacent to the boundary.

Extension to multi-dimensional cases.

The NRBC strategy is extended to the multi-dimensional case by working with the normal velocity component. In practice, the velocity vector $\mathbf{V}_b$ of the boundary cell is projected onto the outward unit normal $\mathbf{n}$ of the face between the boundary cell and the ghost cell: $V_b = \mathbf{V}_b \cdot \mathbf{n}$. This normal velocity component is then used as input in the set of equations (32), ensuring that the NRBC strategy is applied only to the normal flow component.

4 1D and 2D test problems

The NRBC strategy is now tested on 1D and 2D problems to study the method's ability to absorb outgoing disturbances for pure hydrodynamics and hypo-elastic material simulations. For all simulations, the NRBC strategy is compared against the standard Neumann boundary condition (zero-flux outflow), wherein the ghost cell value is assigned directly from the solution within the adjacent computational cell. The test cases presented in this

section are run with the cell-centered Lagrangian scheme detailed in [9], but the NRBC presented also naturally applies to staggered schemes.

4.1 1D piston test

This numerical test section starts with a simple 1D compression problem. A compressible fluid (or material) is confined within a closed domain and driven by the motion of a rigid piston. The domain is initially at rest with uniform pressure and density. A sudden movement of the piston generates a compression wave that propagates through the medium. The spatial domain is set to $[0, 1]$, and a constant velocity is enforced at the left boundary.

Pure hydrodynamics results

A one-dimensional domain filled with a diatomic perfect gas ($\gamma = 1.4$) is considered. The domain is discretized using 100 computational cells, and a CFL number of 0.25 is used. The simulation is carried out up to a final time of $t^f = 0.4$. At the left boundary, a constant velocity of 2 is imposed. The initial conditions are set to uniform pressure and density, both equal to 1. In Figure 1, the numerical solutions obtained using the NRBC strategy and a standard Neumann condition are displayed at times $t = 0.08$ (left wave), $t = 0.16$ (middle wave), and $t = 0.4$ (right wave) working with a mesh of 100 cells. As expected, both solutions coincide prior to the interaction of the wave with the right boundary. This confirms that the wave propagation inside the domain is not affected by the choice of boundary treatment. Ideally, a NRBC should allow outgoing waves to exit the computational domain without generating spurious reflections or incoming disturbances. In practice, it is observed that the presented NRBC simulation allows the wave to exit the domain with less perturbation than the Neumann boundary condition. The NRBC approach clearly outperforms the Neumann boundary strategy. It is also worth noting that both simulations require comparable computational time. Finally, Figure 2 shows the density profiles at time $t = 0.4$ obtained with meshes of 50 (green), 100 (black), 200 (blue), and 400 (red) cells. The right figure corresponds to a Neumann boundary condition applied on the right boundary, while the left figure displays the results obtained with the non-reflecting boundary condition (NRBC). For this discontinuous solution (as well as for the other cases studied in this work), neither boundary condition appears to converge toward a perfect NRBC, i.e., one with no spurious reflection. Nevertheless, for any given mesh, the NRBC provides better re-

sults than the Neumann condition.

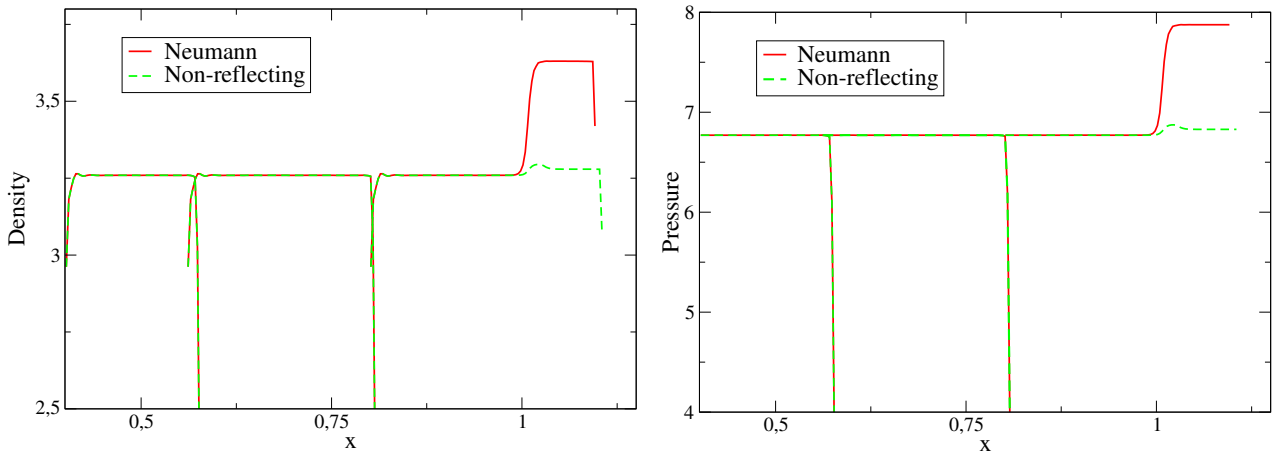

Figure 1: Density (left figure) and pressure (right figure) profiles obtained at times $t = 0.08$ (left wave), $t = 0.16$ (middle wave), and $t = 0.4$ (right wave) with 100 cells. Right boundary condition: Neumann (in red) and NRBC (in green).

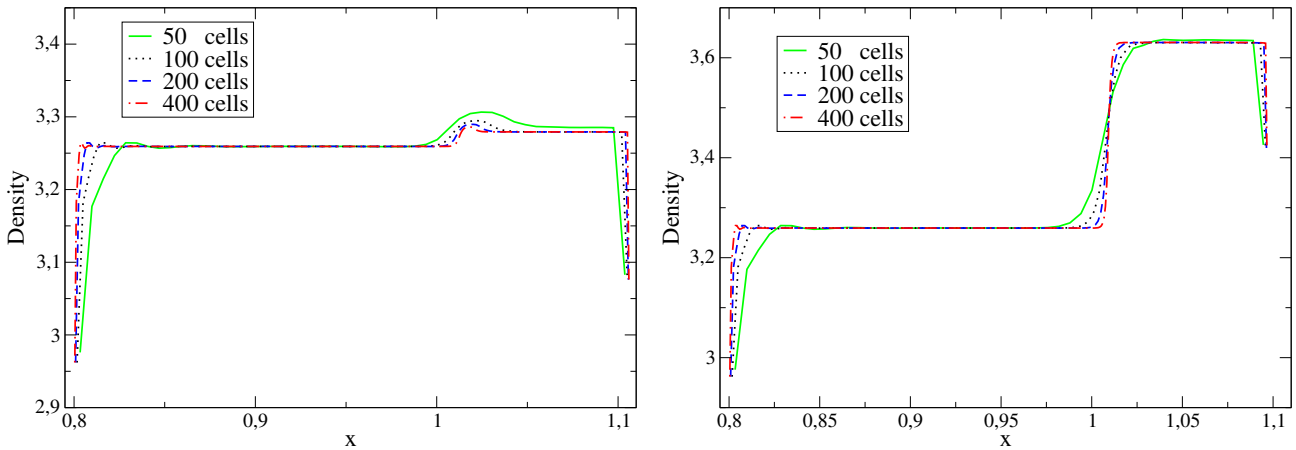

Figure 2: Density profiles at time $t = 0.4$ obtained with meshes of 50 (green), 100 (black), 200 (blue), and 400 (red) cells. The right boundary condition is set to Neumann (right figure) and to the proposed NRBC condition (left figure).

Solid material (hypo-elasticity) results

We now consider a solid material made of aluminum. The computational domain is discretized with 100 cells, and a CFL number of 0.25 is used. The simulation is carried out until a final time of $t^f = 2 \times 10^{-4}$ seconds. On the left boundary, a constant velocity of 800 m/s is imposed. The initial pressure and density are respectively set to 10^{-5} Pa and 2785 kg/m^3. The material behavior is modeled using a Mie-Grüneisen equation of state (see the first section of the document), characterized by the following parameters: $\rho_0 = 2755$ kg/m^3, $a_0 = 5328$ m/s, $\Gamma_0 = 2$, and $s = 1.338$. In addition, the solid response includes a shear modulus $\mu = 27.6 \times 10^9$ Pa and a yield stress $Y^0 = 300 \times 10^6$ Pa. The numerical results obtained using both the NRBC and the standard Neumann condition are presented in Figure 3 at times $t = 1.2 \times 10^{-4}$ (left wave) and $t = 2 \times 10^{-4}$ (right wave) with 100 cells. It is observed that working with the Neumann boundary condition results in a larger portion of the outgoing wave being reflected back into the computational domain. In contrast, the NRBC attenuates the observed spurious reflections more effectively. For this test, it enables a more consistent representation of the wave propagation near the boundary.

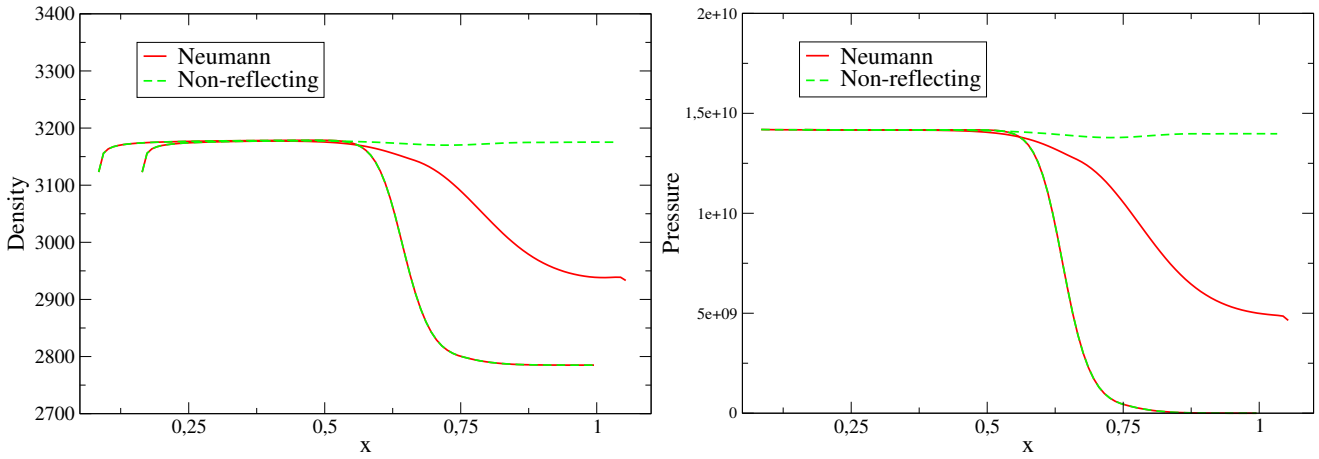

Figure 3: Density (left figure) and pressure (right figure) profiles obtained at times $t = 1.2 \times 10^{-4}$ (left wave) and $t = 2 \times 10^{-4}$ (right wave) with 100 cells. Right boundary condition: Neumann (in red) and NRBC (in green).

4.2 2D diverging shock wave

The second numerical experiment studies the propagation of a diverging cylindrical shock wave. A compressible fluid (or material) is modeled within a two-dimensional, closed square domain defined by $[-0.5, 0.5] \times [-0.5, 0.5]$. Non-reflecting (or Neumann-type) boundary conditions are applied uniformly along all boundaries. The computational domain is discretized using a uniform mesh consisting of 200×200 cells. The initial conditions consist of uniform pressure and density profiles throughout the domain, while the initial velocity field is specified as follows:

$$\boldsymbol{V}(x, y, t = 0) = \begin{cases} (V_0 \cos(\theta), V_0 \sin(\theta)), & \text{if} \quad r < R, \\ 0, & \text{if} \quad r \geq R, \end{cases} \tag{34}$$

where $r = \sqrt{x^2 + y^2}$ and $\theta = \arctan(y/x)$. The velocity magnitude V_0 is chosen depending on the material, and we set $R = 0.1$ for the radius of the velocity disk profile.

Pure hydrodynamics results

A diatomic perfect gas is considered ($\gamma = 1.4$). For this test, the CFL number is set to 0.45 with a final time $t^f = 1.25$. The velocity magnitude is chosen to be $V_0 = 2$, while the initial pressure and density profiles are equal to 1. In Figure 4, the numerical pressure obtained with the NRBC strategy (right column) and the Neumann approach (left column) are displayed at times $t = 0.125$ (top), $t = 0.3125$ (middle), and $t = 0.375$ (bottom) by working with 200×200 cells. These conditions are applied on all boundaries. As expected, before the wave comes into contact with the boundaries, both simulations are identical. It is also observed that a perturbation comes back inside the domain when working with the standard Neumann strategy. Squared pressure profiles are obtained with the Neumann approach, while they remain more circular with the NRBC ones.

Solid material (hypo-elasticity) results

The same aluminum material used in the one-dimensional test is now considered. The simulation is conducted with a CFL number of 0.45, and the final simulation time is set to $t^f = 1.5 \times 10^{-4}$ s. The initial velocity magnitude is prescribed as $V_0 = 800$ m/s, while the initial pressure and density are set to 10^{-5} Pa and 2785 kg/m^3. The equation of state is given by the Mie-Grüneisen model with the following parameters: $\rho_0 = 2755$ kg/m^3, $a_0 = 5328$

m/s, $\Gamma_0 = 2$, and $s = 1.338$. A shear modulus of $\mu = 27.6 \times 10^9$ Pa and a yield stress of $Y^0 = 300 \times 10^6$ Pa are used. In Figure 5, the numerical pressure obtained with the NRBC strategy (right column) and the Neumann approach (left column) are displayed at times $t = 0.6 \times 10^{-4}$ (top), $t = 0.9 \times 10^{-4}$ (middle), and $t = 1.05 \times 10^{-4}$ (bottom), by working with 200×200 cells. These conditions are applied on all boundaries. The observations are similar to those given for the pure hydrodynamic case: a larger perturbation comes back inside the domain when working with the standard Neumann strategy. For this test also, squared pressure profiles are observed with the Neumann approach, while they remain more circular with the NRBC methodology.

4.3 Shock wave in a quarter of a hollow cylinder

This last test investigates the propagation of a shock wave in a curved two-dimensional domain. The domain consists of a quarter-section of a hollow cylinder, with inner and outer radii of 0.02 and 0.03, respectively. A compressible fluid (or material) confined within this region is compressed via a pressure imposed on the left boundary. Initially, the medium is at rest with uniform pressure and density. The imposed boundary pressure generates a compression wave that propagates through the material. For these simulations, the domain is discretized using a mesh of 100×100 cells. A NRBC is applied on the right boundary of the domain, while zero-velocity conditions are enforced on both the top and bottom boundaries.

Pure hydrodynamics results

The initial conditions for the fluid are identical to those used in the first test. The chosen CFL number is equal to 0.9, and the final time of the simulation is $t^f = 0.2$. For this test, a pressure of 1.1 is enforced on the left boundary. In Figure 6, the pressure numerical profiles obtained with the NRBC strategy and the Neumann approach are displayed at times $t = 0.08$ (top), $t = 0.12$ (middle), and $t = 0.16$ (bottom). A Neumann condition or the NRBC is applied on the right boundary. For this new test, it is also observed that the perturbation coming back from the right boundary inside the domain is larger with the standard Neumann strategy.

Solid material (hypo-elasticity) results

For this last test, the chosen CFL number is equal to 0.45, and the final time of the simulation is $t^f = 10^{-5}$ s. For this test, a pressure of 2×10^5

Pa is enforced on the left boundary. The initial pressure and density are respectively set to 10^5 Pa and 2785 kg/m^3. The equation of state is given by the Mie-Grüneisen model with the following parameters: $\rho_0 = 2755$ kg/m^3, $a_0 = 5328$ m/s, $\Gamma_0 = 2$, and $s = 1.338$. A shear modulus of $\mu = 27.6 \times 10^9$ Pa and a yield stress of $Y^0 = 300 \times 10^6$ Pa are used. In Figure 7, the pressure numerical solution obtained with the NRBC strategy and the Neumann approach are displayed at times $t = 4 \times 10^{-6}$ (top), $t = 6 \times 10^{-6}$ (middle), and $t = 8 \times 10^{-6}$ (bottom). The observations are similar to those given for the other tests: it is observed that the perturbation coming back from the right boundary inside the domain is larger when working with the standard Neumann strategy. This demonstrates the superiority of the NRBC presented methodology.

5 Conclusion

In this study, a non-reflecting boundary condition (NRBC) methodology has been presented by adapting Giles' approach [5] to the updated Lagrangian formalism. The strategy is compatible with most standard updated Lagrangian schemes. By leveraging the system's eigenstructure, a simple condition is derived to suppress incoming waves at the domain boundaries. In practice, solving the nonlinear scalar equation yields a solution that can be used to enforce the non-reflecting boundary condition (NRBC) in a Lagrangian code. The numerical section demonstrates that the NRBC outperforms the standard Neumann (zero-flux) boundary condition in absorbing outgoing disturbances for both pure hydrodynamics and hypo-elastic simulations. These numerical results demonstrate the effectiveness of the NRBC strategy as a boundary treatment for updated Lagrangian solvers. Future work may explore the coupling with multi-physics problems.

References

[1] G. Carré, S. Del Pino, B. Després, and E. Labourasse. A cell-centered Lagrangian hydrodynamics scheme on general unstructured meshes in arbitrary dimension. *J. Comput. Phys.*, 228:5160–5183, 2009.

[2] B. Després and C. Mazeran. Lagrangian gas dynamics in dimension two and Lagrangian systems. *Arch. Ration. Mech. Anal.*, 178:327–372, 2005.

[3] B. Engquist and A. Majda. Absorbing boundary conditions for the numerical simulation of waves. *Mathematics of Computation*, 31(139):629–651, 1977.

[4] B. Engquist and A. Majda. Radiation boundary conditions for acoustic and elastic wave calculations. *Communications on Pure and Applied Mathematics*, 32(3):313–357, 1979.

[5] Michael B. Giles. Non-reflecting boundary conditions for euler equation calculations. *AIAA Journal*, 28(12):2050–2058, 1990.

[6] D. Givoli. Non-reflecting boundary conditions: A review. *J. Comp. Phys.*, 94(1):1–29, 1991.

[7] D. Givoli and N. Beny. High-order non-reflecting boundary scheme for time-dependent waves. *J. Comp. Phys.*, 186(1):24–46, 2003.

[8] S.K. Godunov, A. Zabrodine, M. Ivanov, A. Kraiko, and G. Prokopov. Résolution numérique des problèmes multi-dimensionnels de la dynamique des gaz. *Éditions Mir Moscou*, 1979.

[9] S. Guisset, G. Damour, and J. Breil. Cell-centered indirect Arbitrary Lagrangian-Eulerian numerical strategy for solving 3D gas dynamics equations. *J. Comp. Phys.*, 505:112903, 2024.

[10] M.E. Gurtin, E Fried, and L. Anand. The mechanics and thermodynamics of continua. *Cambridge University Press*, 2009.

[11] G.R. Liu and Y.T. Liu. Efficient modeling of wave propagation in complex media using mesh-free methods. *Computers & Structures*, 83(10-11):785–805, 2005.

[12] P.-H. Maire, R. Abgrall, J. Breil, and J. Ovadia. A cell-centered Lagrangian scheme for two-dimensional compressible flows problems. *SIAM J. Sci. Comput.*, 29:1781–1824, 2007.

[13] R. Menikoff. Equations of state and fluid dynamics. *Technical Report LA-UR-07-3989, Los Alamos National Laboratory*, 2007.

[14] P.-H. Maire, R. Abgrall, J. Breil, R. Loubère and B. Rebourcet. A nominally second-order cell-centered Lagrangian scheme for simulating

elastic-plastic flows on two-dimensional unstructured grids. *J. Comput. Phys.*, 235:626–665, 2013.

[15] T.J. Poinsot and L.K. Sanjiva. Boundary conditions for direct simulations of compressible viscous flows. *J. Comp. Phys.*, 101(1):104–129, 1992.

[16] J. von Neumann and R.D. Richtmyer. A method for the numerical calculations of hydrodynamical shocks. *J. Appl. Phys.*, 21:232–238, 1950.

[17] M.L. Wilkins. Calculation of elastic plastic flow. *Methods Comput. Phys.*, 3:211–263, 1964.

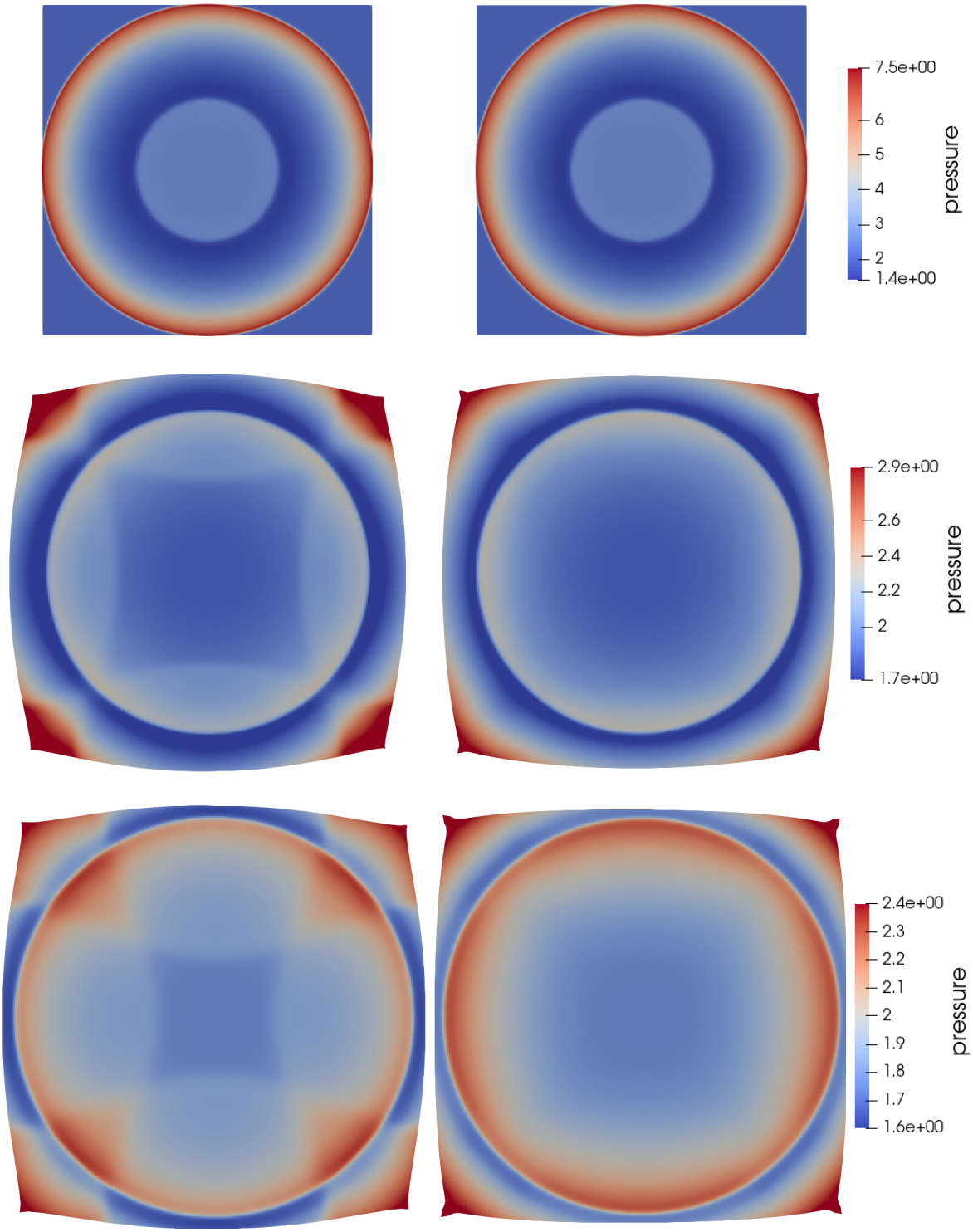

Figure 4: Pressure profile obtained with 200×200 cells at times $t = 0.125$ (top), $t = 0.3125$ (middle), and $t = 0.375$ (bottom). Neumann conditions (left) and NRBC (right) are applied on all boundaries.

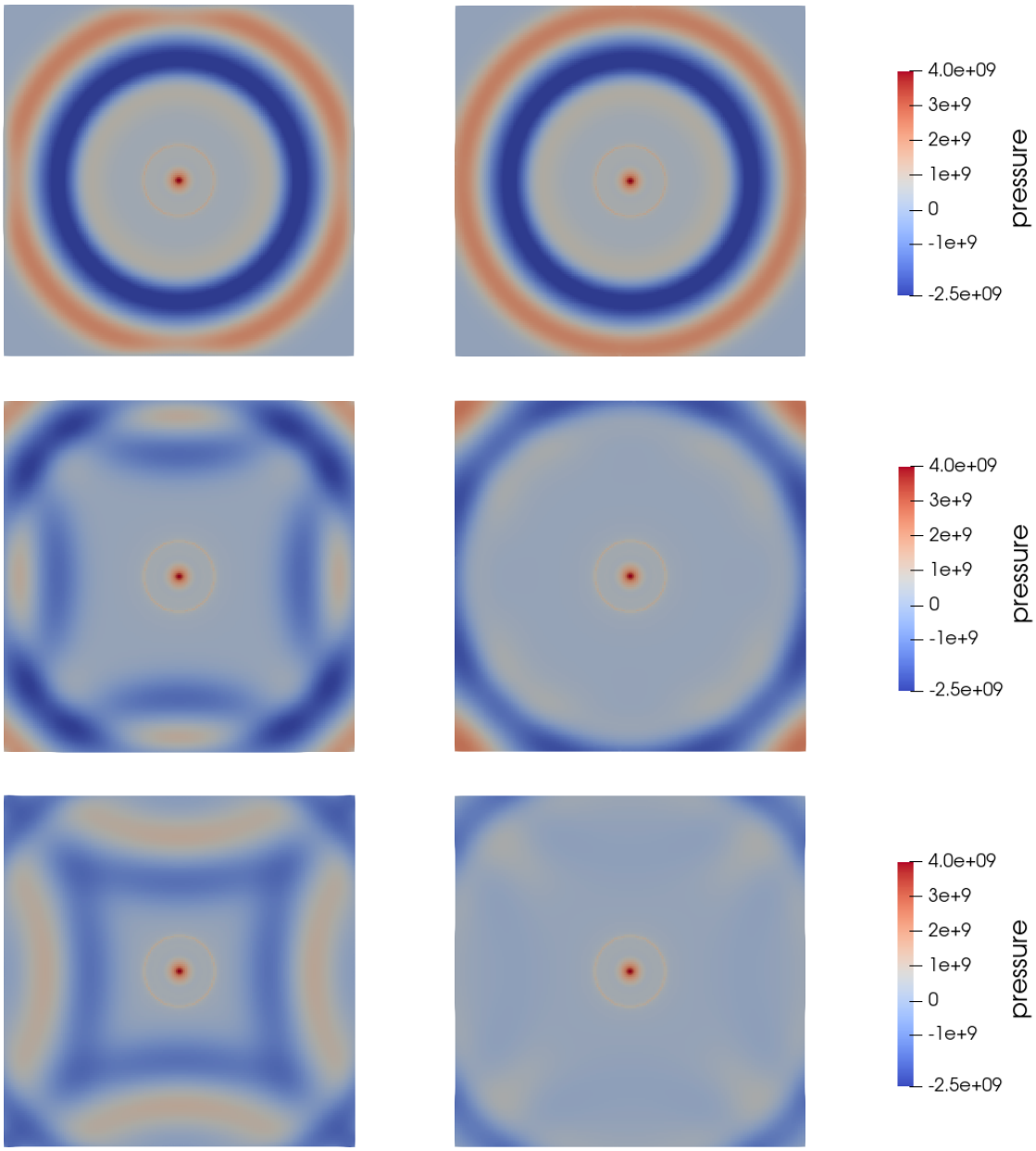

Figure 5: Pressure profile obtained with 200×200 cells at times $t = 0.6 \times 10^{-4}$ (top), $t = 0.9 \times 10^{-4}$ (middle), and $t = 1.05 \times 10^{-4}$ (bottom). Neumann conditions (left) and NRBC (right) are applied on all boundaries.

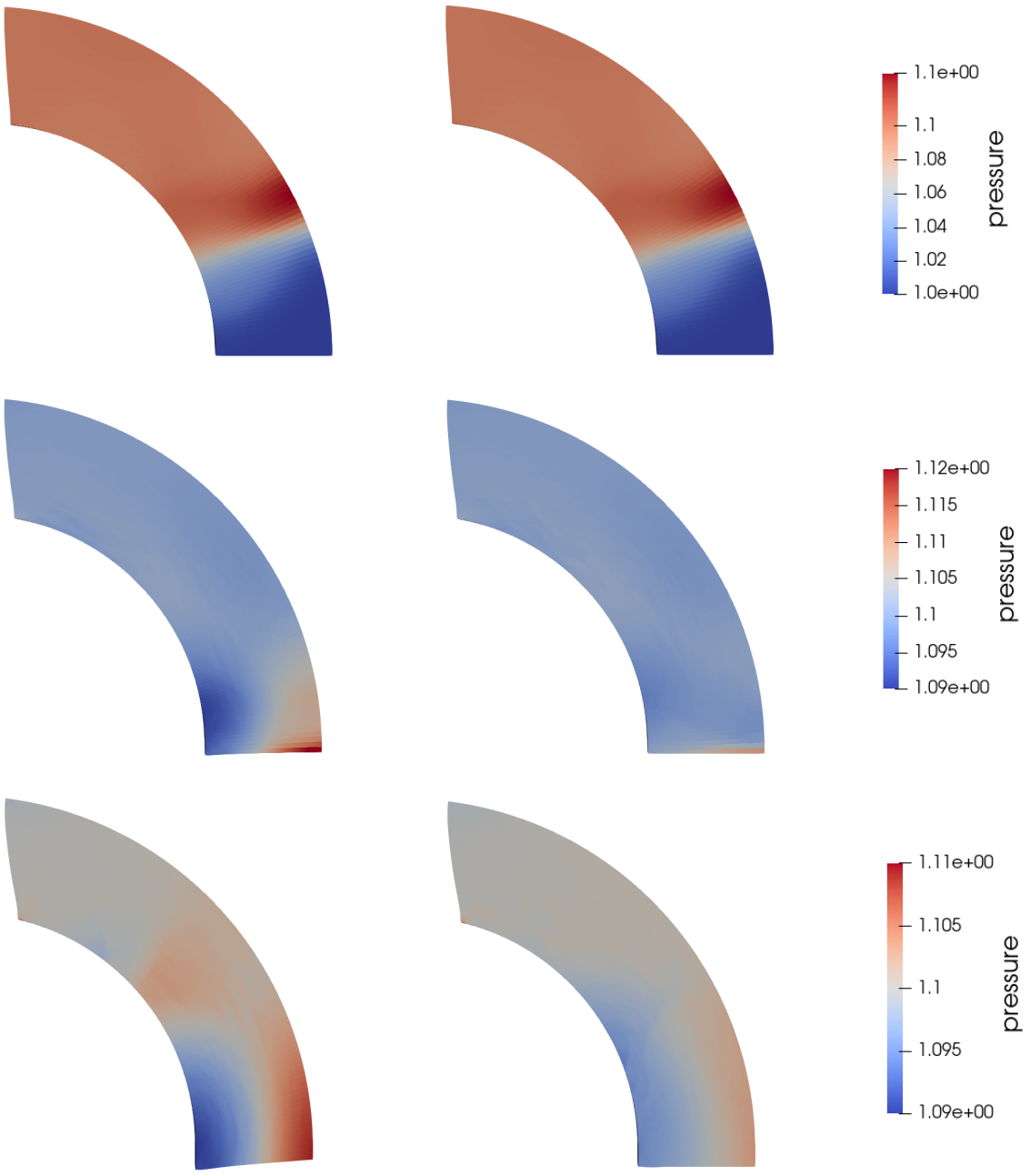

Figure 6: Pressure profile obtained with 100×50 cells at times $t = 0.08$ (top), $t = 0.12$ (middle), and $t = 0.16$ (bottom). Right boundary condition: Neumann (left) and NRBC (right).

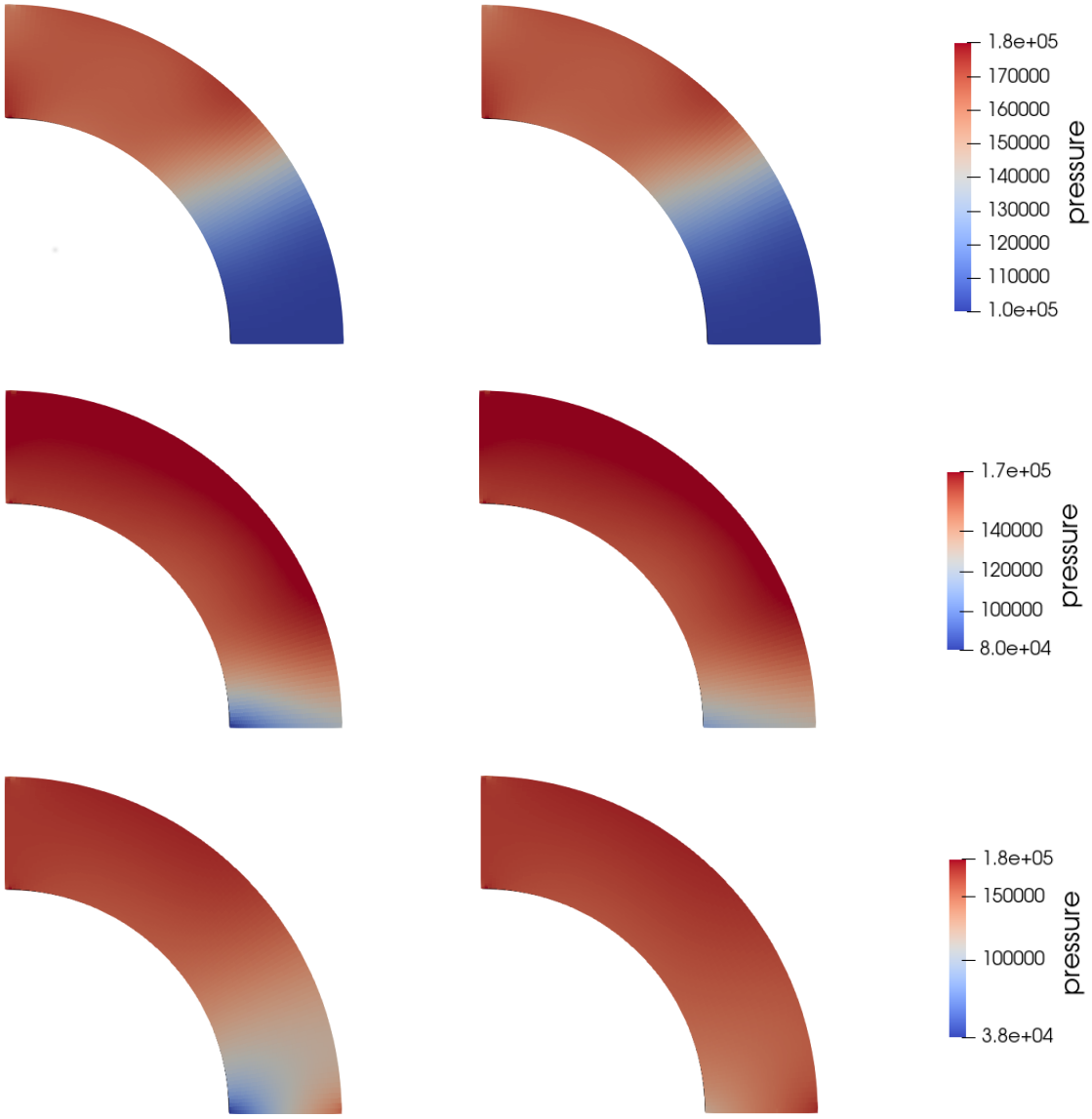

Figure 7: Pressure profile obtained with 100×50 cells at times $t = 4 \times 10^{-6}$ (top), $t = 6 \times 10^{-6}$ (middle), and $t = 8 \times 10^{-6}$ (bottom). Right boundary condition: Neumann (left) and NRBC (right).